JOURNAL OF AIRCRAFT
Vol. 46, No. 6, November–December 2009

Three-Dimensional Aerodynamic Design of Low-Wave-Drag Supersonic Biplane Using Inverse Problem Method

D. Maruyama,* K. Matsushima,† K. Kusunose,‡ and K. Nakahashi§
Tohoku University, Sendai 980-8579, Japan

DOI: 10.2514/1.40313

In supersonic flight, airfoils generate strong sonic boom and wave drag accompanied by shock waves and expansion waves. The Busemann biplane is representative of an airfoil that has the possibility of realizing low drag. With the aim of realizing a new concept of supersonic transport, aerodynamic design and analysis are discussed based on computational fluid dynamics. Traditional biplane airfoils were extended to three-dimensional wings with a design Mach number of 1.7. Euler simulations of three-dimensional biplane wings of several configurations were conducted. Because of the existence of wing tips, three-dimensional biplane wings do not perform as well as two-dimensional biplane airfoils. This is because the areas affected by Mach cones originated from the wing tips, which precludes the occurrence of an appropriate pressure wave interaction. Thus, the wing tip area has a large drag coefficient. To overcome these problems, a tapered wing is herein considered. After parametric studies, a wing planform was determined, the taper ratio and aspect ratio of which were 0.25 and 5.12, respectively. Aerodynamic design of wing section shapes of the three-dimensional tapered biplane wing was conducted using an inverse-problem method. The designed biplane wing shows a better lift-to-drag ratio performance than the two-dimensional flat-plate airfoil in the range where the lift coefficient is more than 0.17. Tapered wings were also found to have several span sections that achieve better performances than two-dimensional biplane airfoils.

Nomenclature

b	=	semispan length
C_D	=	drag coefficient of the three-dimensional wing
C_L	=	lift coefficient of the three-dimensional wing
C_d	=	drag coefficient of the two-dimensional airfoil
C_{df}	=	friction drag coefficient of the two-dimensional airfoil in Navier–Stokes simulations
C_{dp}	=	pressure drag coefficient of the two-dimensional airfoil in Navier–Stokes simulations
C_l	=	lift coefficient of the two-dimensional airfoil
C_p	=	pressure coefficient
c	=	chord of the two-dimensional airfoil
c_{mid}	=	position of the midchord at the wing tip of the three-dimensional wing
c_{root}	=	chord at the wing root of the three-dimensional wing
c_{tip}	=	chord at the wing tip of the three-dimensional wing
c_1, c_2	=	Busemann coefficients
$f(x)$	=	airfoil geometry
h	=	gap between two elements of the biplane
L/D	=	lift-to-drag ratio of the three-dimensional wing
l/d	=	lift-to-drag ratio of the two-dimensional airfoil
M_∞	=	freestream Mach number
Re	=	Reynolds number
S	=	reference area
t	=	airfoil thickness
x	=	streamwise coordinate
y	=	spanwise coordinate
z	=	vertical coordinate
α	=	angle of attack
γ	=	ratio of specific heats
ε	=	inclination relative to the freestream direction
θ	=	$\mathrm{d}f/\mathrm{d}x$-α
AR	=	aspect ratio

Presented as Paper 0289 at the 46th AIAA Aerospace Sciences Meeting and Exhibit, Grand Sierra Resort Hotel (Formerly Reno Hilton) Reno, NV, 7–10 January 2009; received 8 September 2008; revision received 14 May 2009; accepted for publication 2 July 2009.

*Graduate Student, Department of Aerospace Engineering; daigo@ad.mech.tohoku.ac.jp. Student Member AIAA.

†Associate Professor, Department of Aerospace Engineering; kisam@ad.mech.tohoku.ac.jp. Senior Member AIAA.

‡Invited Visiting Professor, Institute of Fluid Science; currently Senior Research Scientist, Technical Research and Development Institute, Ministry of Defense, Tachikawa 190-8533, Japan. Member AIAA.

§Professor, Department of Aerospace Engineering. Associate Fellow AIAA,

I. Introduction

LOW noise capability and high fuel efficiency are critical for the next generation of supersonic transport. In a word, it is necessary to develop an airplane characterized by low boom and low drag. Over 70 years ago, using the favorable interaction between two wing elements, Busemann proposed a biplane configuration in which these two conditions were satisfied [1,2]. The wave drag due to airfoil thickness can be nearly eliminated using a biplane configuration that promotes favorable wave interactions between the two neighboring airfoil elements (wave drag being defined as a force of resistance on the airfoil due to the generation of shock waves). Licher extended the idea to reduce the wave drag due to lift [3]. Moeckel predicted that the performance of a biplane airfoil can exceed that of the zero-thickness single flat-plate airfoil [4]. In experiments on supersonic biplanes, Ferri found flow choking with a concomitant hysteresis phenomenon at off-design conditions, which are disadvantages of supersonic biplanes [5]. Recently, employing both computational fluid dynamics (CFD) and experimental approaches, a supersonic biplane project has been commenced to realize the next generation of supersonic transport [6–18]. We have previously designed a two-dimensional biplane airfoil that has lower wave drag than the single flat-plate airfoil at a sufficient lift condition of $M_\infty = 1.7$ [9,18]. It has also been shown that flow choking and resulting hysteresis, which are serious issues of supersonic biplanes under off-design conditions, could be avoided by using slats and flaps for the high-lift device [12,13,18]. However, these are findings of two-dimensional analysis, whereas for a practical flight three-dimensional wings must be considered. Although various approaches for analyzing three-dimensional biplane wings were used in the past [19–21], many issues for realizing a practical supersonic transport remain.

In this paper, we discuss the design of a lifting three-dimensional biplane wing using a newly devised inverse-design method. The objective is to realize a three-dimensional supersonic biplane wing with high aerodynamic performance using CFD code in Euler (inviscid flow) mode. In the extension from two-dimensional biplane airfoils to three-dimensional wings, a great amount of drag can be expected to be produced around the wing tip [11,15]. How traditional biplane airfoils such as the Busemann biplane and the Licher biplane can be extended to a practical biplane wing will be discussed. Two subjects will be described in this paper. One is investigation of the extension of two-dimensional biplane airfoils to three-dimensional wings, in which we discuss analysis of three-dimensional wings to which the biplane airfoils were applied and selection of the wing planform. The other is design of a three-dimensional wing using the inverse-problem method. To attain further improvement of aerodynamic performance of a three-dimensional biplane wing for practical flight, the two-dimensional designed biplane airfoil is applied to the selected planform.

II. Background of Two-Dimensional Supersonic Biplane Airfoils

The total wave drag of an airfoil can be divided into two components. One is the wave drag due to its thickness and the other is that due to lift. An appropriate biplane configuration can reduce both of these, especially most of the wave drag due to airfoil thickness. In this section the theory of the biplane concept for wave-drag elimination will be introduced and discussed using CFD.

A. Busemann Biplane (Reduction of Wave Drag Due to Volume)

The Busemann biplane, proposed by Busemann in 1935, is an airfoil that has the possibility of realizing low-drag supersonic flight [1,2]. As mentioned in the Introduction, the wave drag is divided into two main components. One is the wave drag due to airfoil thickness (or volume) and the other is that due to lift. The wave drag due to airfoil thickness can be significantly reduced by using the concept of the Busemann biplane.

Figure 1 shows the theory of the Busemann biplane with a zero-lifting diamond airfoil. The diamond airfoil has zero lift, but has wave drag due to airfoil thickness corresponding to its thickness-chord ratio. Busemann showed that the wave drag of the diamond airfoil can be eliminated by simply splitting the diamond airfoil into two elements and positioning them in such a way that the waves generated by those elements cancel each other out. However, the reflected shock waves are not completely eliminated by the expansion waves because of nonlinearity of expansion waves [8].

B. Licher Biplane (Reduction of Wave Drag Due to Lift)

Although the Busemann biplane cannot reduce the wave drag due to lift, it can reduce that due to airfoil thickness. In 1955, Licher extended the concept of the Busemann biplane to reduce the wave drag due to lift [3]. Generally, in supersonic flight when there is no interference with waves between the two elements of a biplane airfoil, the wave drag due to lift can be reduced by half compared with the case of a monoplane airfoil [7,8].

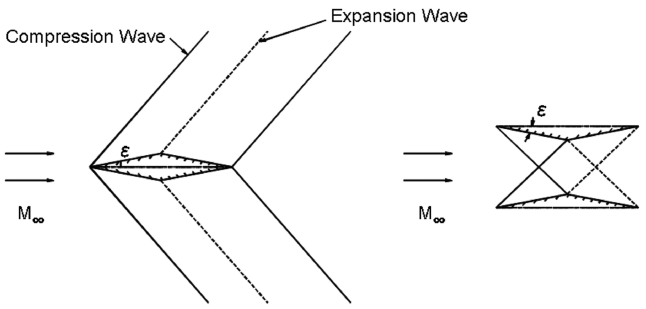

Fig. 1 Wave cancellation effect of Busemann biplane for reduction of wave drag due to airfoil thickness.

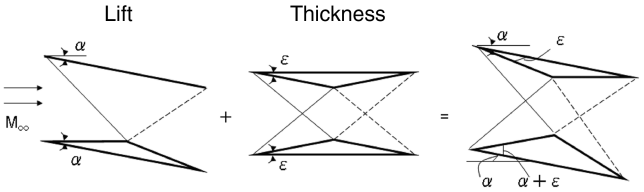

Fig. 2 Extension to Licher biplane for reduction of wave drag due to lift.

Figure 2 shows the theory of the Licher biplane. The Licher biplane is obtained by combining a lifting biplane airfoil that has partial interference of waves between its two elements (interference of the shock wave at the leading edge of the upper element and the expansion wave at the midchord of the lower element) with the Busemann biplane. As a result, in the Licher biplane, wave drag due to lift can be reduced by two-thirds in addition to the reduction of drag due to airfoil thickness (effects of the Busemann biplane).

C. Designed Biplane Airfoil

The Licher biplane airfoil was previously modified to achieve higher aerodynamic performance [8,9,18]. An inverse-problem method was used as the design method. With this method an airfoil with a specified C_p distribution can be determined. Details of the theory and the flow solver for simulation are presented in the next section.

Using the Busemann biplane as the baseline model, the total thickness-chord ratio of the upper and lower elements was set at 0.10 (each element is 0.05). Therefore, ε in Fig. 1 was determined to be 5.71 deg. Under the condition of a freestream Mach number of 1.7, the gap between the two elements was set at 0.5. (It is defined so that shock waves generated at the leading edges hit the edge of the midchord.) The Licher biplane airfoil has almost the same parameters as the Busemann biplane airfoil. The α (on biplanes, the angle of the lower surface of the lower element against the freestream direction was defined as an angle of attack) in Fig. 2 was set at 1 deg, and ε was 5.71 deg. The aerodynamic performance of the Busemann biplane airfoil is $C_l = 0.000$ and $C_d = 0.00218$, and that of the Licher biplane airfoil is $C_l = 0.0812$, $C_d = 0.00449$, and $l/d =$ 18.1. It is important to remember that, in this study, lift and drag coefficients of biplanes were calculated based on the chord length c.

The Licher biplane airfoil was modified by the inverse-design method. Figure 3 shows geometries and C_p distributions of the designed biplane airfoil and the Licher biplane airfoil as an initial model. The designed biplane airfoil was termed the designed airfoil. The aerodynamic performance of the designed airfoil is $C_l = 0.115$, $C_d = 0.00531$, and $l/d = 21.7$. The C_p distributions between the initial and designed biplane airfoil differ in pressure peaks at midchords on both elements and the C_p distribution around the trailing edge on the upper element. Pressure distributions near the trailing edge (of the upper element) were specified to maximize the pressure recovery at the trailing edge. This is the most important factor in creating more lift without a large increase of wave drag. Figure 4 shows C_p visualization of the designed airfoil. Favorable interference of shock waves and expansion waves between the two elements can be observed.

Figure 5 shows a drag polar diagram of various two-dimensional airfoils. It includes the characteristics of the two-dimensional zero-thickness single flat-plate airfoil, which has the lowest drag in monoplanes at this Mach number ($M_\infty = 1.7$) and has only wave drag due to lift as drag. The designed airfoil achieved lower wave drag than the flat-plate airfoil at $C_l > 0.14$. Details of the biplane can be found in [8,9,18].

D. Viscous Effects

For practical flight viscous effects have to be taken into account. The skin friction of a single flat plate is estimated using the following incompressible turbulent boundary-layer formulas [22]:

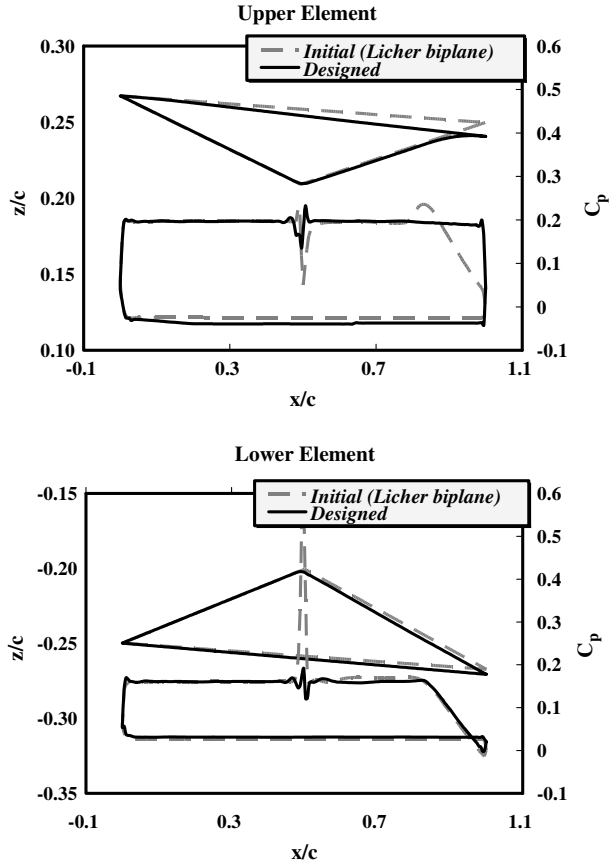

Fig. 3 Geometries and C_p distributions of the Licher biplane as an initial model and the designed airfoil.

$$C_{df} = 2C_f \tag{1}$$

where

$$C_f = \frac{0.027}{(Re)^{1/7}} \tag{2}$$

Here the symbol Re denotes the Reynolds number based on the flat-plate chord length c. For the conversion to compressible flow, variation of skin friction coefficient with Mach number that is plotted on Fig. 13.10 in [2] is used. The Reynolds number based on the chord length c is set at 30 million. The friction drag coefficients C_{df} of a single airfoil and a biplane airfoil can be estimated to be 0.00369 and 0.00739, respectively.

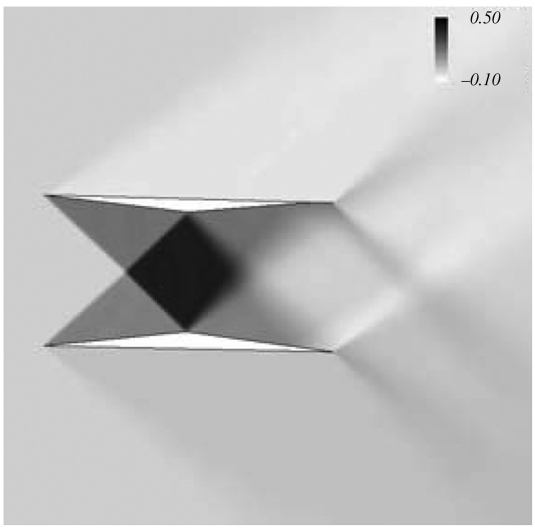

Fig. 4 C_p visualization of the designed airfoil.

Several Navier–Stokes simulations of the diamond airfoil, the Busemann biplane airfoil, and the designed airfoil were conducted [8,9,18]. A one-equation turbulence model by Spalart–Allmaras [23] is adopted to treat turbulent boundary layers for viscous flow computations. Table 1 shows their aerodynamic performance in Navier–Stokes simulations at Reynolds number 30 million. The friction drag coefficients C_{df} are almost the same in all cases and also agree well with that from the flat-plate theory. The increment of the friction drag coefficient compared with single airfoils is at most around 0.0040, which is smaller than the decrease of the wave-drag coefficients. Even though the wet area of a biplane is twice of that of a monoplane such as a diamond airfoil, the total drag coefficient of a biplane airfoil is about one-third of that of a monoplane.

III. Computational Method

In this research wing configurations were designed using an inverse-design system. With this system new wing configurations are obtained by alternating use of flow analysis and the inverse-problem method. A flow solver, the inverse-problem method, and the inverse-design system that integrates them are discussed in the following subsections.

A. Flow Solver

A flow solver named Tohoku University aerodynamic simulation code using a three-dimensional unstructured grid [24,25] was used to evaluate aerodynamic performance. In the simulation, the Euler/Navier–Stokes equations were solved by a finite volume cell-vertex scheme. The lower/upper symmetric Gauss–Seidel (LU-SGS) implicit method for an unstructured grid [26] was used for the time integration. In this research, all analyses were conducted using the Euler equations.

B. Inverse-Design System

With an inverse-problem approach, in general, the geometry of a wing section can be determined given a specified (target) pressure distribution. Because the pressure distribution of an airfoil and its shock wave strength are directly related, an inverse-problem approach will be a highly appropriate tool for finding a biplane configuration to achieve minimum wave drag under a given lift condition. Consequently, an inverse-design system using the small perturbation form of the second order equation to relate pressure to local flow deflection angles has been developed [9,10,27].

In this design system, the geometry of an airfoil $f(x)$ is related to its pressure distribution by the following local oblique shock relation [2]:

$$C_p = c_1\theta + c_2\theta^2 \tag{3}$$

where θ and C_p represent the local flow deflection angle ($\mathrm{d}f/\mathrm{d}x$-α) and pressure coefficient, respectively. Along the airfoil surface we assume the local flow is tangential to the surface contour of the airfoil. The symbols c_1 and c_2 are the Busemann coefficients, given as

$$c_1 = \frac{2}{\sqrt{M_\infty^2 - 1}}, \qquad c_2 = \frac{(M_\infty^2 - 2)^2 + \gamma M_\infty^4}{2(M_\infty^2 - 1)^2}$$

α is the angle of attack of the airfoil, and x and γ represent the airfoil-chord direction (see Fig. 6) and the ratio of specific heats, respectively.

Figure 7 illustrates the iterative process of the method. First, the flowfield around an initial configuration is analyzed to obtain its initial pressure distribution. Next, an inverse-problem solver is employed to calculate the x derivative of the correction value for the airfoil geometry, $\mathrm{d}\Delta f \pm / \mathrm{d}x$; this x derivative is related to the difference between the target and the current pressure distributions, denoted as ΔC_p (C_p residual). Specifically, the geometry correction

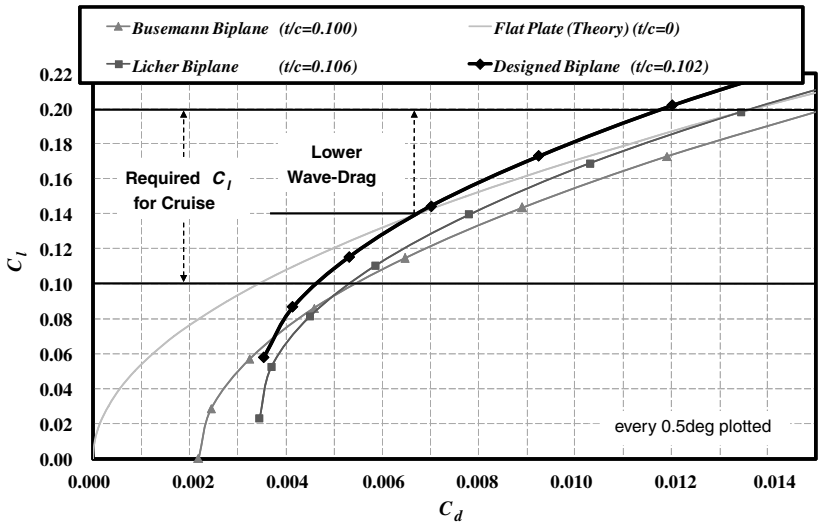

Fig. 5 Drag polar diagram of two-dimensional biplane airfoils and flat-plate airfoil.

term Δf (see Fig. 6) comes from ΔC_p, using the small perturbation forms ($C_p \to C_p + \Delta C_p$ and $f \to f + \Delta f$) of Eq. (3)

$$\Delta Cp_+ = c_1\left(\frac{\mathrm{d}\Delta f_+(x)}{\mathrm{d}x}\right) + 2c_2\left(\frac{\mathrm{d}f(x)}{\mathrm{d}x} - \alpha\right)\left(\frac{\mathrm{d}\Delta f_+(x)}{\mathrm{d}x}\right) + c_2\left(\frac{\mathrm{d}\Delta f_+(x)}{\mathrm{d}x}\right)^2 \tag{4}$$

$$\Delta Cp_- = -c_1\left[\frac{\mathrm{d}\Delta f_-(x)}{\mathrm{d}x}\right] + 2c_2\left[\frac{\mathrm{d}f_-(x)}{\mathrm{d}x} - \alpha\right]\left[\frac{\mathrm{d}\Delta f_-(x)}{\mathrm{d}x}\right] + c_2\left[\frac{\mathrm{d}\Delta f_-(x)}{\mathrm{d}x}\right] \tag{5}$$

Here, $+$ and $-$ indicate the upper and lower surfaces, respectively. The airfoil geometry is updated by integrating the geometry correction terms:

$$f_\pm^{\text{update}}(x) = f_\pm(x) + \int_0^x \frac{\mathrm{d}\Delta f_\pm}{\mathrm{d}\xi}(\xi)\,\mathrm{d}\xi \tag{6}$$

where the symbol 0 indicates the x coordinate of the leading edge of the airfoil. In this approach, however, it is obvious that there is no guarantee of obtaining an airfoil that has a closed trailing edge. Therefore, a further (but minor) modification of the specified target pressure distribution may be needed to close the trailing edge. Finally, we analyze the flowfield of the updated airfoil geometry. An optimal airfoil design can be found through the repetition of this process.

IV. Selection of Planform of Three-Dimensional Supersonic Biplane Wing at Zero-Lift Conditions

For a practical flight, three-dimensional wings have to be considered. As mentioned in the Introduction, the drag of supersonic biplanes is expected to increase mainly because of the existence of wing tips. For example, on rectangular wings, the section drag around their wing tips is higher than that at other sections. In this section, an optimal planform of a Busemann biplane wing (at zero-lift condition) is discussed. Therefore, all analyses performed in Sec. IV are under the zero-lift conditions. The thickness-chord ratio (t/c) is 0.10. The reference area of wings in this section is fixed at

Table 1 Aerodynamic performance in Navier–Stokes simulations

	α, deg	C_l	C_{dp}	C_{df}	C_d	l/d
Diamond	0	0	0.0292	0.00394	0.0332	0
	2	0.104	0.0329	0.00414	0.0370	2.8
Busemann	0	0	0.00185	0.00777	0.00962	0
	2	0.116	0.00639	0.00780	0.0142	8.2
Designed	1.19	0.116	0.00479	0.00794	0.0127	9.1

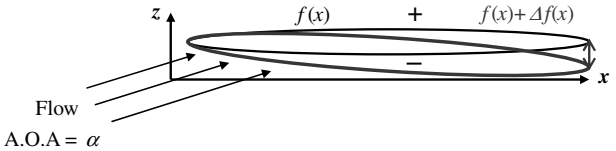

Fig. 6 Airfoil geometries and perturbed geometries.

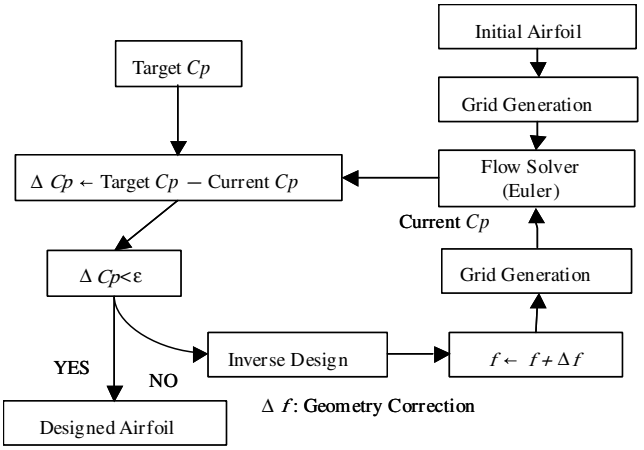

Fig. 7 Design cycle of inverse-design system.

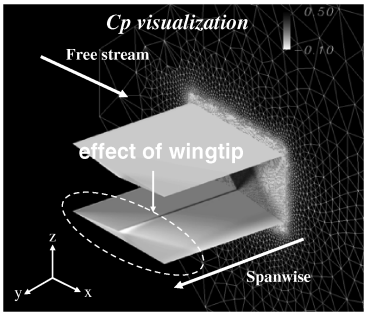

Fig. 8 Mesh and C_p visualizations of a rectangular Busemann biplane wing (reference area 1).

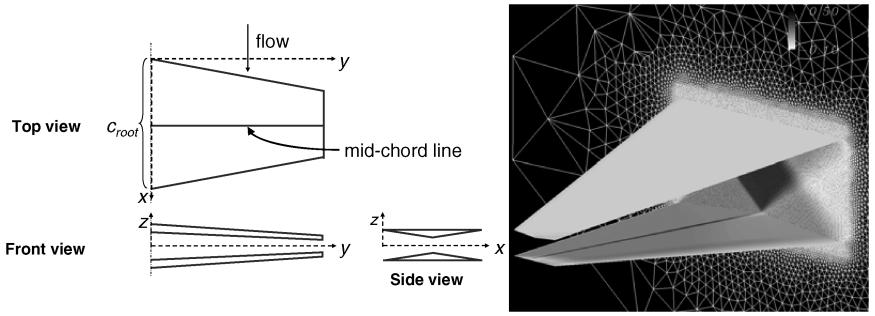

Fig. 9 Orthographic drawing and mesh and C_p visualizations of a tapered Busemann biplane wing (reference area 1).

one. Design of a three-dimensional lifting biplane wing using the inverse-design method is discussed in the next section.

A. Background of Three-Dimensional Busemann Biplane Wing

First, the phenomena and problems that are produced when two-dimensional supersonic biplane airfoils are extended to three-dimensional wings are introduced. Figure 8 shows C_p visualization of a three-dimensional rectangular Busemann biplane wing. The reference area is one. Therefore, the semispan length and the aspect ratio are 1 and 2, respectively. The wing-sectional configuration is the same as that of the Busemann biplane airfoil shown in Sec. II.C (the total thickness-chord ratio is 0.10.). The number of nodes used in our CFD analysis is about 1.10 million. In Fig. 8 the effects of Mach cones from the wing tips, that is, an increase of wave drag, can be seen. The C_D of the wing is 0.00685. It is very high compared with the C_d of the two-dimensional result ($C_d = 0.00218$).

To reduce the Mach cone effects from the wing tips, a tapered wing was considered. Figure 9 shows surface C_p visualization of a three-dimensional tapered Busemann biplane wing. The reference area is 1 and the taper ratio is 0.25. Therefore, the semispan length and the aspect ratio are 1.6 and 5.12, respectively. The C_D of the wing is 0.00300, which is lower than that of the previously mentioned rectangular wing. Figure 10 shows spanwise C_d distributions of the rectangular and the tapered biplane wings, as well as the C_d of the two-dimensional result. Effects of Mach cones from the wing tips were significantly reduced by using the tapered wing, although weak shock cones generated from the wing root can be seen. This tapered wing has another merit in section C_d, namely, the C_d distributions in the midwing areas not affected by these Mach cones are lower than that of the two-dimensional result. In the next section geometric parameters of a planform based on a tapered Busemann biplane wing are discussed.

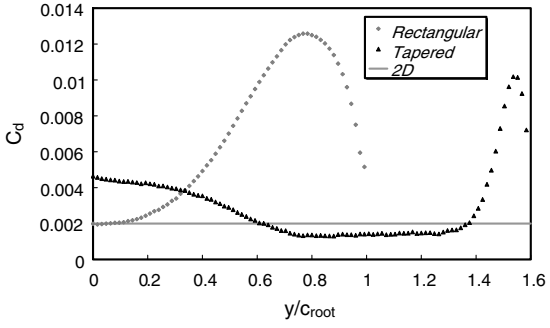

Fig. 10 Spanwise C_d distributions of rectangular and tapered Busemann biplane wings (zero-lift conditions).

B. Selection of Sweep Angle

In this subsection characteristics with changes of a sweep angle of a tapered wing are discussed, the taper ratio being set at 0.25. Here the sweep angle is defined as the angle of the wing leading edge to the freestream. Figure 11 shows C_D characteristics with changes of the sweep angle. The sweep angle was evaluated in this study by a coordinate of the midchord apex at the wing tip ($C_{\mathrm{mid}}/C_{\mathrm{root}}$, see Fig. 11). When $C_{\mathrm{mid}}/C_{\mathrm{root}}$ (defined in Fig. 11) is around 0.5 or less, C_D is minimum.

Figure 12 illustrates simple diagrams of two wings termed case 1 and case 2, and spanwise C_d distributions of these two wings. Case 1 has no sweep ($C_{\mathrm{mid}}/C_{\mathrm{root}} = 0.125$). Case 2 has a sweep angle and its midchord line is normal to the freestream direction ($C_{\mathrm{mid}}/C_{\mathrm{root}} = 0.5$). As shown in Fig. 11, case 2 has a lower C_D than case 1. Figure 13 shows C_p visualizations of the inner surfaces of case 1 and case 2, including comparison of C_p distributions of the two wings at 50% semispan stations and the two-dimensional result. It can be seen that C_p distributions of case 1 and case 2 differ from that of the two-dimensional result in the midchord to the trailing edge region although the sectional geometry of these three are identical. This is due to the difference of their effective (wing-sectional) geometries to the flow as shown in Fig. 12. Based on the result given in Fig. 11, we selected case 2 for selection of the sweep angle.

C. Selection of Taper Ratio

The characteristics of the C_D of a tapered wing with changes of the taper ratio were examined. The midchord of the wing was fixed to be normal to the freestream direction (case 2, $C_{\mathrm{mid}}/C_{\mathrm{root}} = 0.5$ in Fig. 11). Figure 14 shows C_D and the aspect ratio characteristics with changes of the taper ratio when the reference areas of the studied

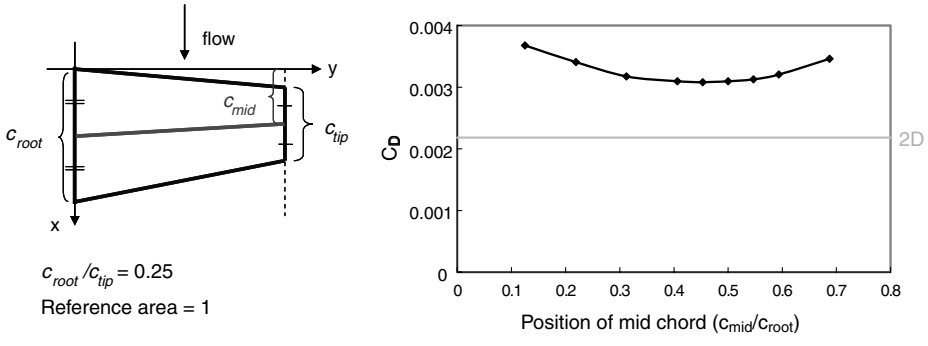

Fig. 11 C_d characteristics with changes of the sweep angle (reference area 1, zero-lift conditions).

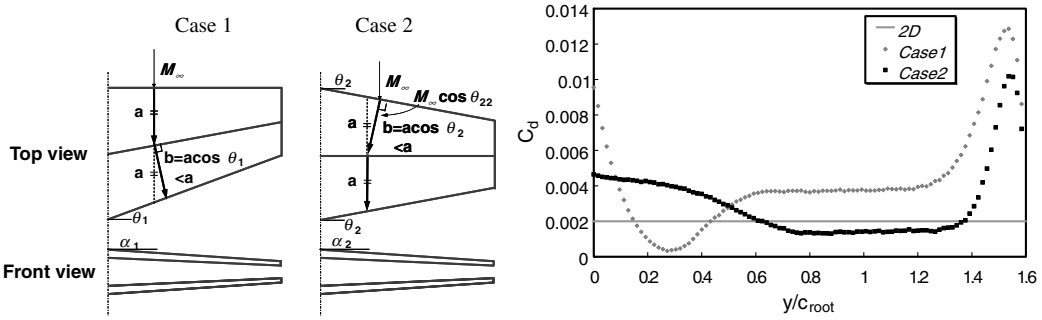

Fig. 12 Simple diagram of interaction of the shock waves and the expansion waves and spanwise C_d distributions of case 1 and case 2 (zero-lift conditions).

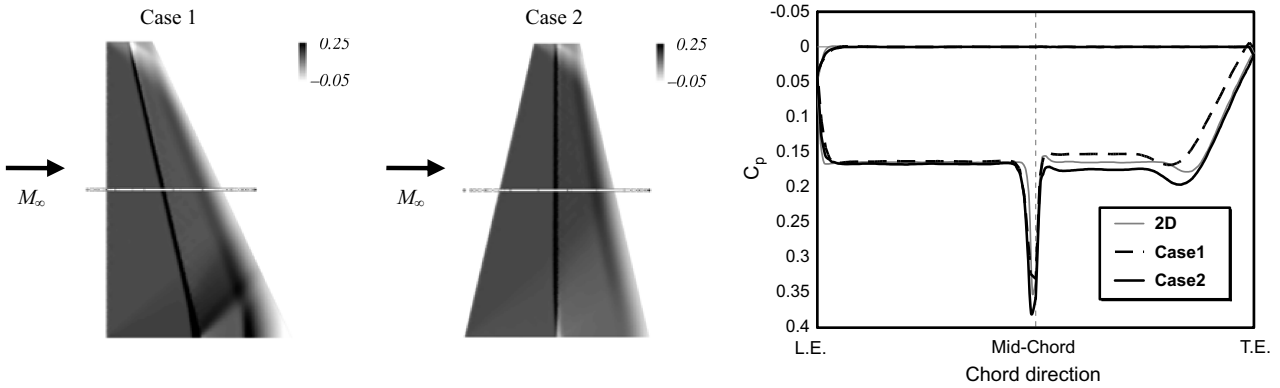

Fig. 13 C_p visualizations of the inner surfaces and C_p distributions at 50% semispan stations (not affected by Mach cones) of case 1 and case 2.

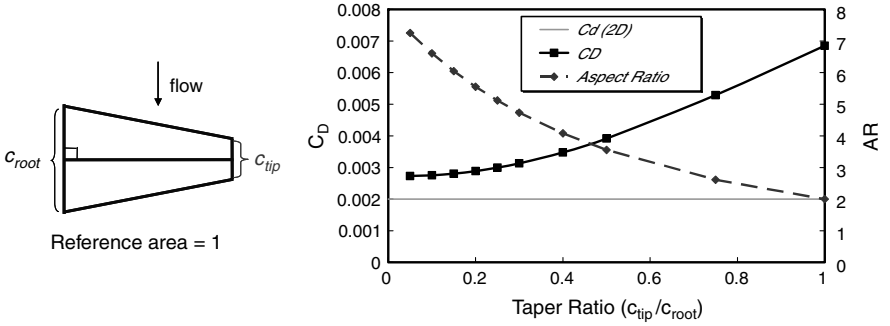

Fig. 14 C_D and aspect ratio characteristics with changes of taper ratio (zero-lift conditions).

wings are fixed to be 1. The smaller the taper ratio is, the lower C_D is. The aspect ratio also increases with decreasing taper ratio. However, C_D does not decrease much when a taper ratio is less than 0.25, whereas the aspect ratio begins to increase rapidly. Furthermore, attention must be paid to structural problems. Therefore, a taper ratio of 0.25 was selected. The aspect ratio is determined to be 5.12. In the next section, the design of a three-dimensional biplane wing with the selected planform (the parameters of which are shown in Table 2) is discussed using the inverse-design approach. It is important to remember that the Busemann biplane wing with this planform has values of $C_D = 0.00300$ at zero-lift conditions.

V. Design of Three-Dimensional Supersonic Biplane Wing Using the Inverse-Problem Method

This section presents the design of three-dimensional biplane wings using the inverse-design method. As a wing planform the tapered wing, the parameters of which are shown in Table 2, was used in this section. Validation of the inverse-design approach to a three-dimensional biplane wing and practical design for a three-dimensional lifting supersonic biplane wing are discussed.

A. Validation of the Inverse-Design Method for a Three-Dimensional Biplane Wing

For the fundamental check of design capability of three-dimensional biplane wings using the inverse-problem method, we examined whether a three-dimensional tapered biplane with arbitrary wing-sectional geometries converged to a known three-dimensional tapered Busemann biplane wing by setting up the C_p distribution of the Busemann biplane wing as a target. This process was conducted at several span stations of the wing simultaneously. A flow chart for the three-dimensional design is illustrated in Fig. 15. As shown in

Table 2 Geometric parameters of the selected wing planform as a baseline model

Parameters	Conditions
Taper ratio	0.25
Aspect ratio	5.12
Semispan length	1.6
Reference area	1
Midchord line	Normal to the freestream

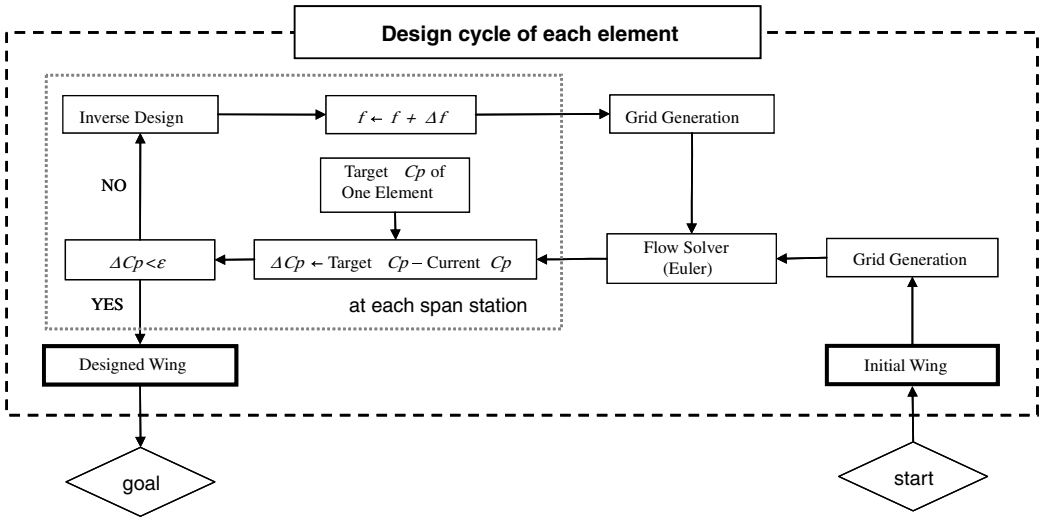

Fig. 15 Design flow chart of one element of a three-dimensional biplane wing.

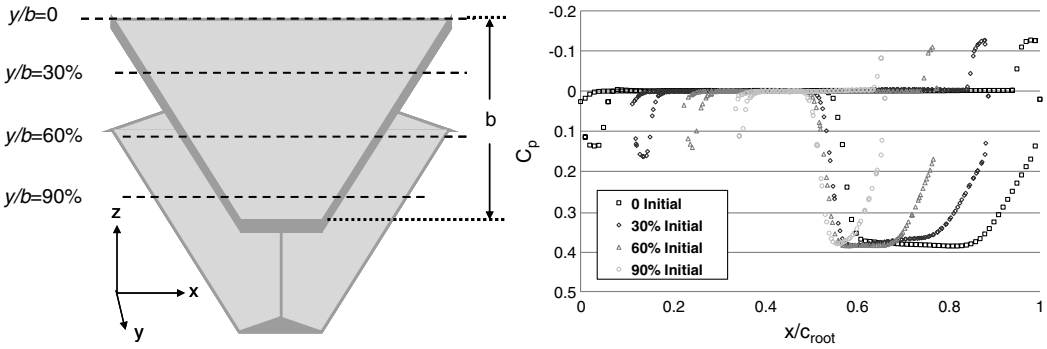

a) Initial configuration and C_p distributions

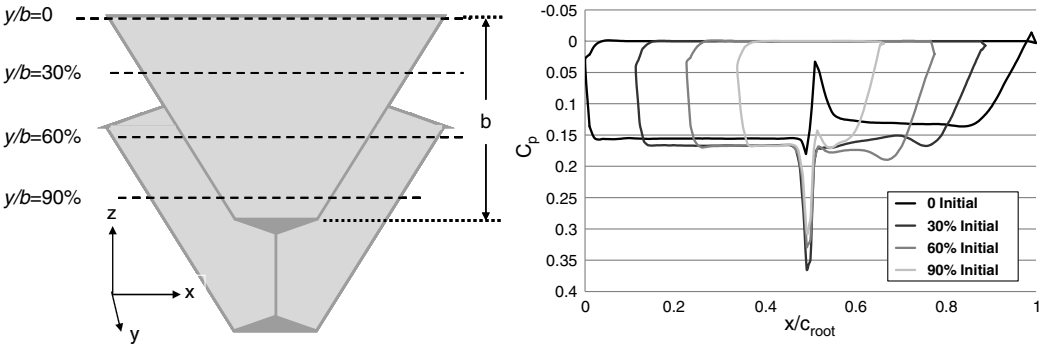

b) Target configuration (tapered busemann biplane) and C_p distributions

Fig. 16 Simple diagrams of initial configuration and its C_p distributions, and tapered Busemann biplane and its C_p distributions as a target.

Fig. 16, the wing with the upper element being a flat plate and the lower one having a tapered Busemann biplane was set to an initial wing configuration. The resulting C_p distributions at 10 span stations from the wing root (represented as $y/b = 0$, b means semispan length) to the 90% span station (represented as $y/b = 90\%$) of the upper element of the designed Busemann biplane were given in Fig. 17 with the specified target C_p distributions (only four sections are described in Figs. 15, 17, and 18). The wing tip configuration of each iteration is defined by using the designed geometry at the 90% span station. The updated wing shape was defined by using the linear interpolation of the designed geometries between those ten span stations. The number of nodes used for the simulation process in this section is about 0.55 million.

Figures 17 and 18 show obtained C_p distributions, geometries after 14 iterations. It was confirmed that they successfully converged at target ones after only 14 iterations of the design procedure.

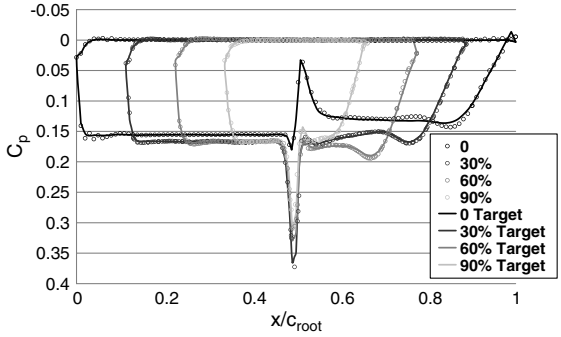

Fig. 17 C_p distributions at some sections of the designed wing after 14 iterations.

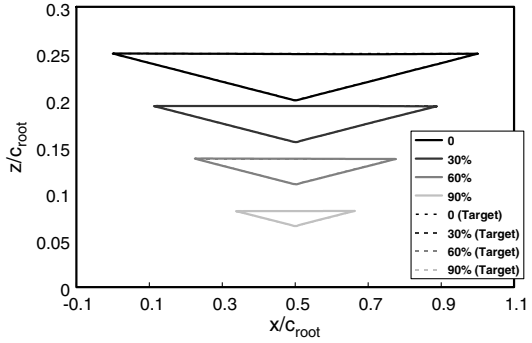

Fig. 18 Geometries at some sections of the designed wing after 14 iterations.

B. Design of a Three-Dimensional Lifting Supersonic Biplane Wing

Practical design of a three-dimensional biplane wing with high L/D at sufficient lift conditions ($C_L > 0.1$) is discussed in this subsection. The previously mentioned inverse-problem method was used for aerodynamic design. In the previous subsection only one element of a biplane wing was designed. Here, design of both the upper and lower elements is discussed. The inverse-design method was applied to each of them alternately (see Fig. 15).

1. *Design Condition*

For the inverse-design approach, an initial wing model needs to be chosen. As a planform of the initial wing, the tapered wing shown in Table 2 was selected. The reference area and the taper ratio are 1 and 0.25, respectively. The semispan length and the aspect ratio are 1.6 and 5.12, respectively. The airfoil configuration of the tapered wing as the initial wing was set using the biplane configuration designed by the inverse-problem method (designed airfoil, see Fig. 3) at each span station of the wing. The wing, termed initial wing, has values of $C_L = 0.111$, $C_D = 0.00621$, and $L/D = 17.9$. The number of nodes used for the simulations is about 1.10 million. The initial wing was set to be the initial model of the inverse-design process. Table 3 shows the aerodynamic performance of the designed airfoil (which is also represented as initial wing with an infinite span) and that of the initial wing.

Table 3 Aerodynamic performance of designed airfoil and initial wing

	Lift coefficient	Drag coefficient	Lift-to-drag ratio
Designed airfoil	0.115	0.00531	21.7
Initial wing	0.111	0.00621	17.9

2. *Design Process*

The inverse-design method was applied to each of the upper and lower elements alternately during the updating of the geometry, the other element being fixed. It was applied at 10 span stations (spanwise, every 10% from 0 to 90%) of each element simultaneously. The design procedure shown in Fig. 15 was carried out for both the upper and lower elements. First, some design iterations were conducted on the upper element until the obtained C_p distributions converged to the target (upper) C_p distributions, the wing configuration of the lower element being fixed. Then the lower element was designed, the configuration of the new designed upper element being fixed. After the design cycle of each element, if the aerodynamic performance at a section of the designed wing did not improve compared with that of the initial wing, the designed section was replaced by the initial one.

3. *Analysis of the Initial Model*

The initial wing was used as the initial model of the inverse-design process. Figure 19 shows C_p visualizations of the inner surfaces and C_p distributions of the initial wing. Let us focus on the C_p distributions of the inner sides (C_p distributions of the lower surface of the upper element and of the upper surface of the lower element). Compared with the C_p distributions of the designed airfoil (see

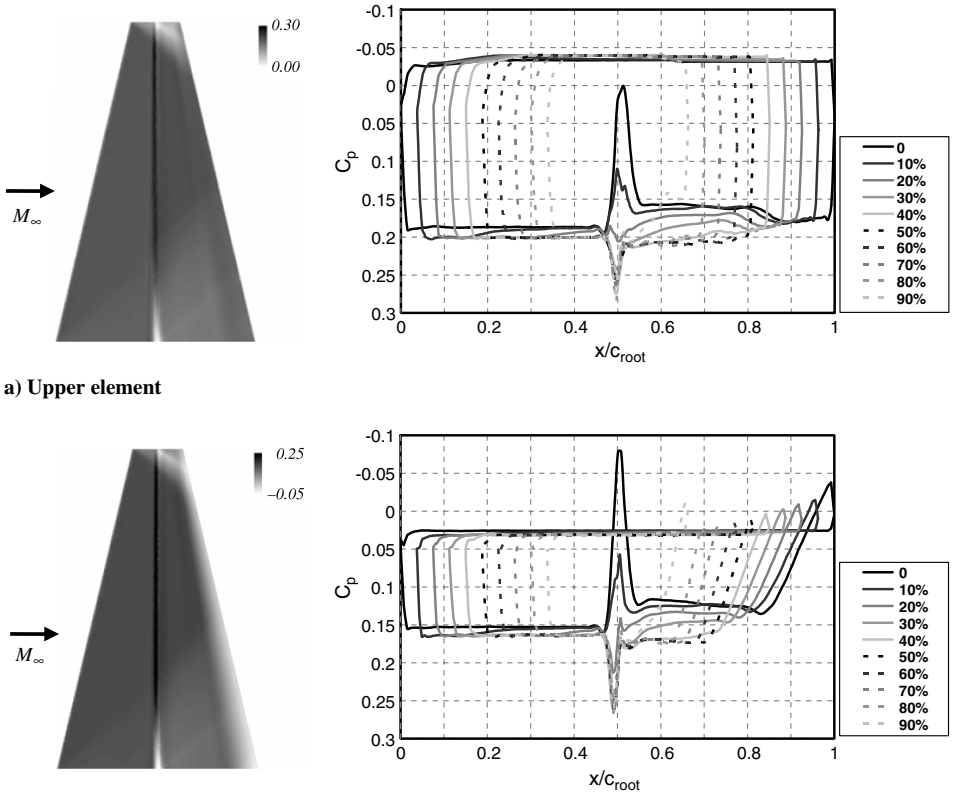

a) Upper element

b) Lower element

Fig. 19 C_p visualizations of the inner surfaces and C_p distributions of the initial wing.

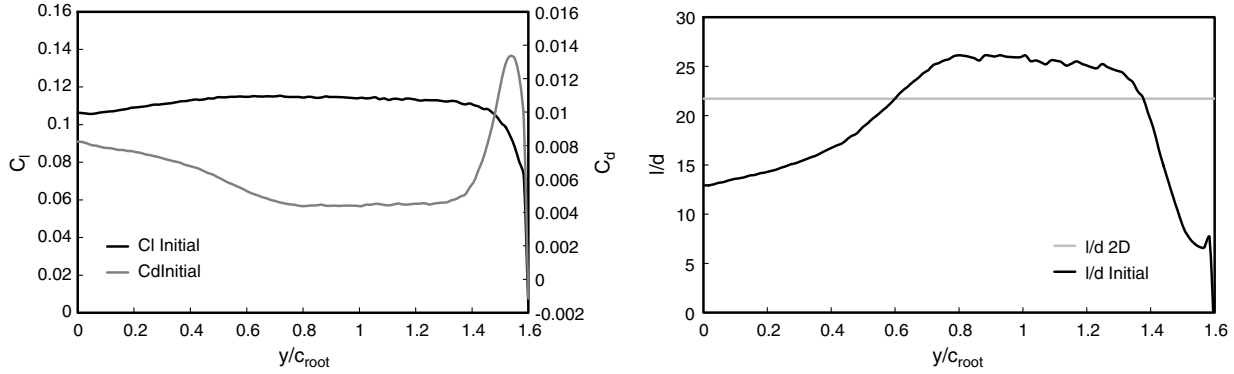

Fig. 20 Spanwise C_l, C_d, and l/d distributions of the initial wing.

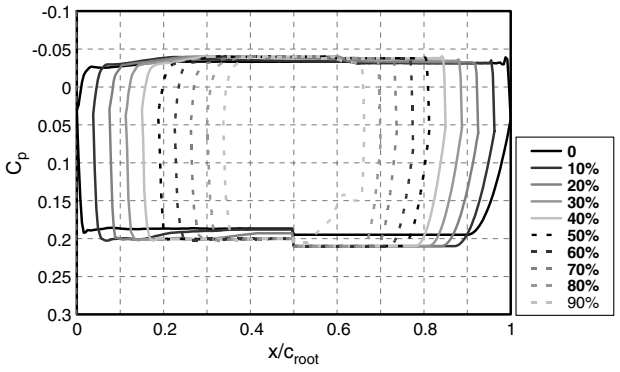

Fig. 21 Target C_p distributions of the upper element.

Fig. 3), large pressure peaks were recognized on both the upper and lower elements. Also the values of the pressure coefficients in the areas not affected by Mach cones generated at the wing root section (y/b of 50–80%) were higher than those in the areas affected by the Mach cones (y/b of 0–40%). On the upper element, shapes of the C_p distributions between the midchords and the trailing edges greatly altered from those of the designed airfoil at each span station.

Figure 20 shows spanwise C_l, C_d, and l/d distributions of the initial wing. It can be observed that the areas affected by Mach cones from the wing root and the wing tip are characterized by poor aerodynamic performance, but those not affected by the Mach cones have a higher lift-to-drag coefficient than that shown by the two-dimensional analysis. These are characteristics of the three-dimensional tapered biplane wings as mentioned in Sec. IV.A. The goal of the design here is to create a biplane wing that has better aerodynamic performance than the initial model by using desirable C_p distributions as target pressures at span stations. Therefore, appropriate target pressure distributions should be determined.

4. *Guideline for Setting Target Pressure Distributions*

To prescribe target pressure distributions for our three-dimensional wing design, we set the following two guidelines. We tried to remove the unnecessary pressure peaks that occurred around the midchord areas in the baseline initial wing. We then extend the

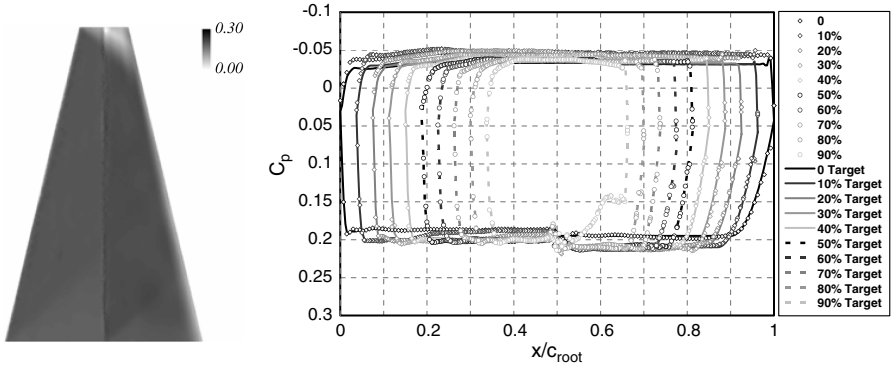

Fig. 22 C_p visualization of the inner surface, and target and obtained C_p distributions of the upper element of the upper designed wing.

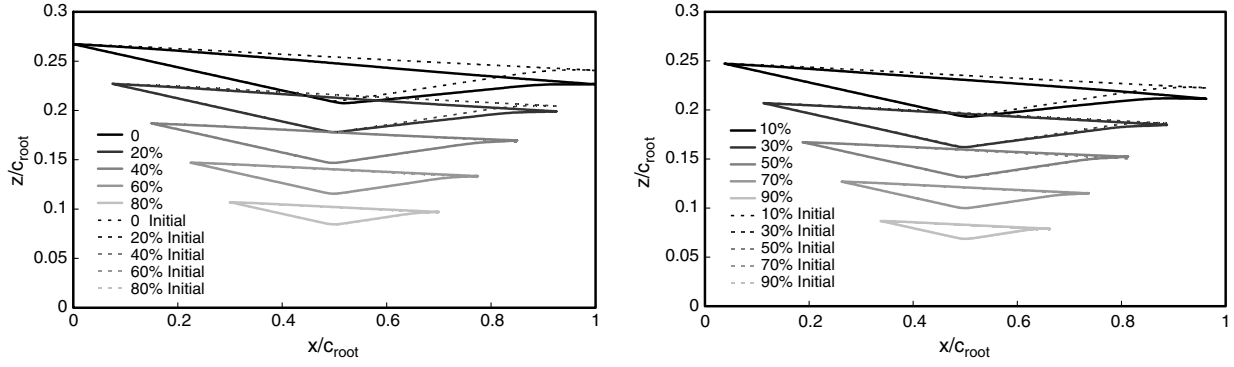

Fig. 23 Designed section geometries of the upper designed wing.

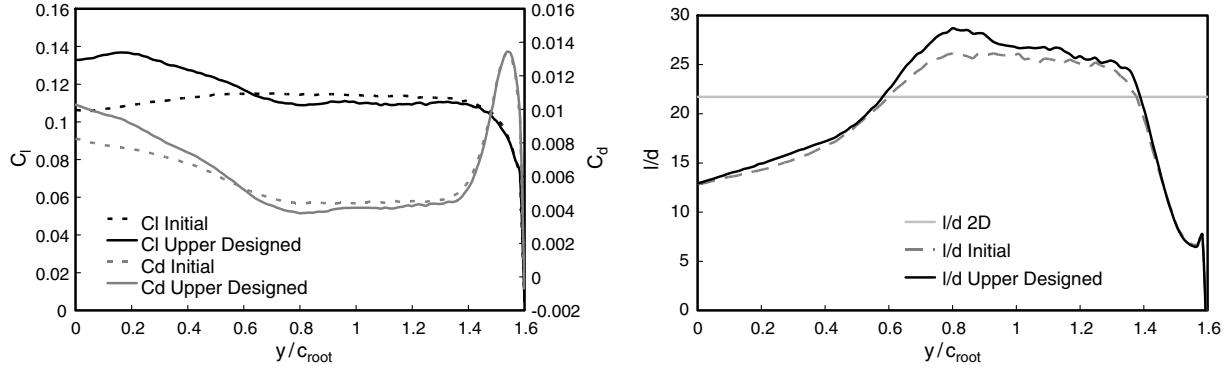

Fig. 24 Spanwise C_l, C_d, and l/d distributions of the upper designed wing.

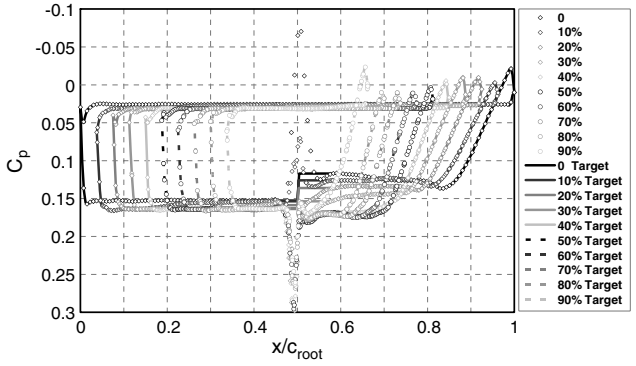

Fig. 25 Target C_p distributions of the lower element and C_p distributions of the lower element of the upper designed wing as initial C_p distributions.

previously discussed better C_p distributions, which are obtained from the midwing region of the initial wing, into the regions near the wing tip and the wing root to improve aerodynamic performance in those regions. It is important to remember that the C_p distributions in those regions are greatly affected by Mach cones generated from the wing tips and the wing root (target pressure distributions for the upper and lower elements used for the three-dimensional wing design are shown in Figs. 21 and 25, respectively).

5. *Design Results*

Let us focus on target C_p distributions and actually obtained C_p distributions from the designed wings. First the upper element was designed. Details of the target C_p distributions of the upper element are shown in Fig. 21. Figure 22 shows the obtained C_p distributions of the designed wing (after 14 iterations of the inverse-design cycle) and the C_p contours of the inner surfaces of the upper wing. This designed wing was termed the upper designed wing. The obtained C_p distributions successfully converged with the target distributions. C_L, C_D, and L/D are 0.120, 0.00662, and 18.1, respectively. L/D was improved with the increase of C_L. Figure 23 shows the designed

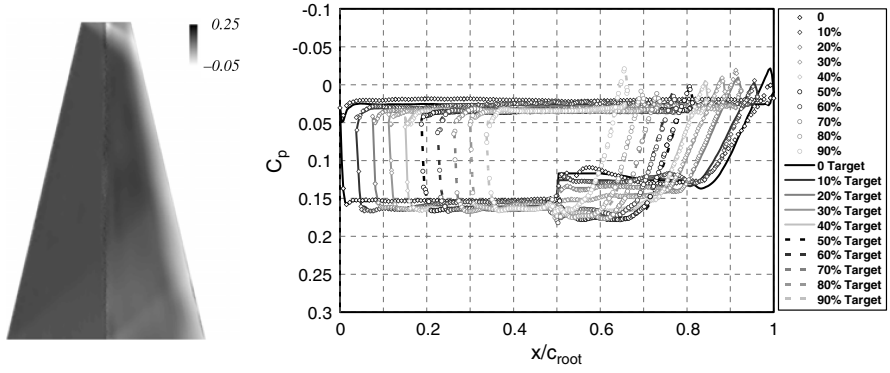

Fig. 26 C_p visualization of the inner surface and target and obtained C_p distributions of the lower element of the upper and lower designed wing.

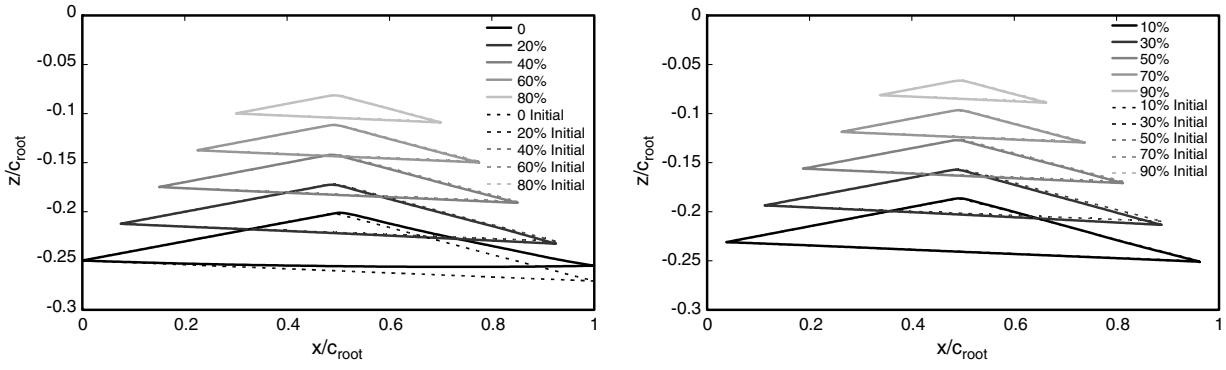

Fig. 27 Designed section geometries of the upper and lower designed wing.

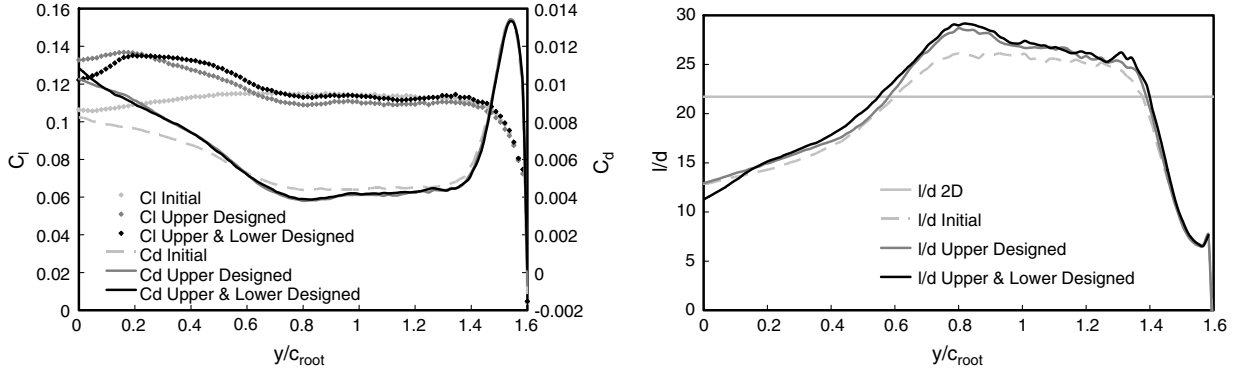

Fig. 28 Spanwise C_l, C_d, and l/d distributions of the upper and lower designed wing.

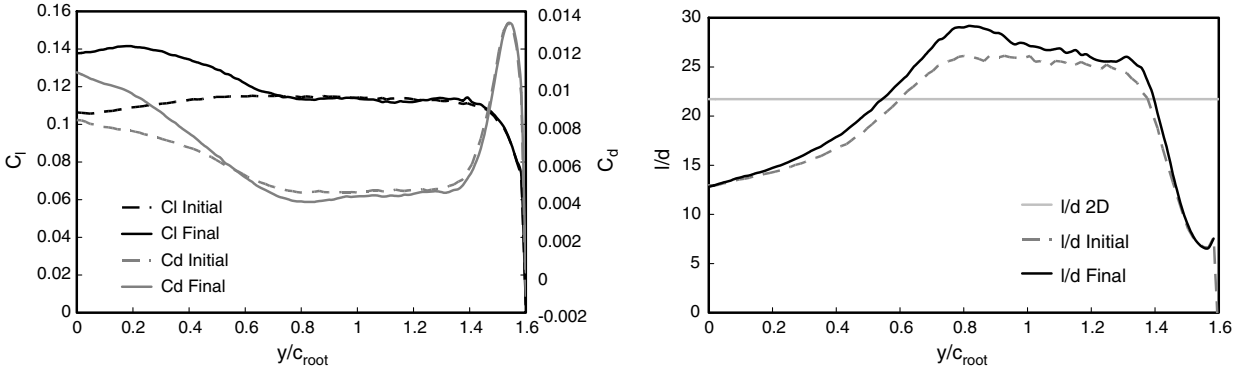

Fig. 29 Spanwise C_l, C_d, and l/d distributions of the final wing.

section geometries of the upper designed wing. Figure 24 shows its spanwise C_l, C_d, and l/d distributions. The geometries around the wing symmetry section were modified to have more angles of attack. Spanwise C_l in the areas affected by Mach cones increased without reductions of the spanwise l/d.

Next the lower element was designed. The C_p distributions of the lower element obtained after 14 iterations of the previously discussed upper element design were used as the initial distributions. The initial and target C_p distributions of the lower element are shown in Fig. 25. As mentioned in the previous subsection, the difference between the initial and the target C_p distributions is only the presence of pressure peaks at the midchords. Figure 26 shows obtained C_p distributions after 14 iterations and C_p visualization of the inner surfaces of the designed biplane wing, which was termed upper and lower designed wing. The pressure peaks were successfully removed. Unfortunately, at the wing root section the C_p distribution around the trailing edge did not converge with the target distributions. The designed wing has C_L, C_D, and L/D of 0.122, 0.00664, and 18.3, respectively. Figure 27 shows designed section geometries of the upper and lower designed wing. Figure 28 shows its spanwise C_l, C_d, and l/d distributions. We obtained an improved result by the lower element design. However, remarkable changes in geometries were not observed except in the symmetry section (0% at the span station). When the geometry of the wing root section was modified, the angle of attack became lower. Spanwise C_l and l/d of the upper and lower designed wing became worse than those of the initial wing, although those in the other sections of the designed wing were much improved. Therefore, we conducted the following modification.

The geometry at the wing root section of the lower element of the upper and lower designed wing was replaced by the initial one. This wing was termed the final wing. Figure 29 shows spanwise C_l, C_d, and l/d distributions, and Fig. 30 shows C_p visualizations of the inner surfaces of the final wing. This wing maintained higher l/d than the initial model at all span stations, and more lift was created in the areas affected by Mach cones originated from the wing root. The final wing has values of $C_L = 0.125$, $C_D = 0.00678$, and $L/D = 18.4$. The design operation was stopped at this point.

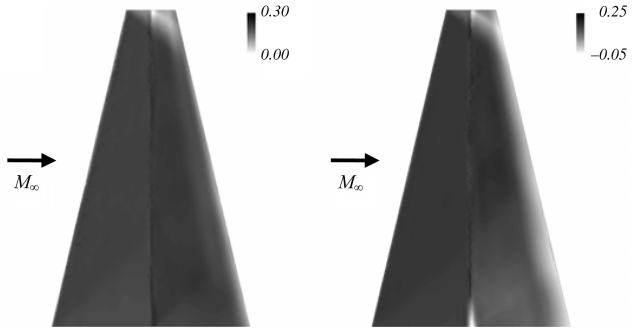

a) Upper element **b) Lower element**

Fig. 30 C_p visualizations of the inner surfaces of the final wing.

6. *Comparison with Other Three-Dimensional Supersonic Biplane Wings*

Table 4 shows the aerodynamic performance of various three-dimensional tapered biplane wings. The designed biplane wings show a higher aerodynamic performance with a lower angle of attack α (which is defined by the angle of the lower surface of the lower element against the freestream direction) than the Busemann and Licher biplane wings. Figure 31 shows a drag polar diagram of the three-dimensional biplane wings, which includes the two-dimensional zero-thickness single flat-plate airfoil shown in Sec. II.C. The two-dimensional flat-plate airfoil can be equated with the

Table 4 Aerodynamic performance of three-dimensional biplane wings

Three-dimensional biplane wing	C_L	C_D	L/D
Busemann biplane wing ($\alpha = 2$ deg)	0.110	0.00706	15.6
Licher biplane wing ($\alpha = 1.5$ deg)	0.107	0.00642	16.7
Initial wing ($\alpha \cong 1$ deg)	0.111	0.00621	17.9
Final wing ($\alpha \cong 1$ deg)	0.125	0.00678	18.4

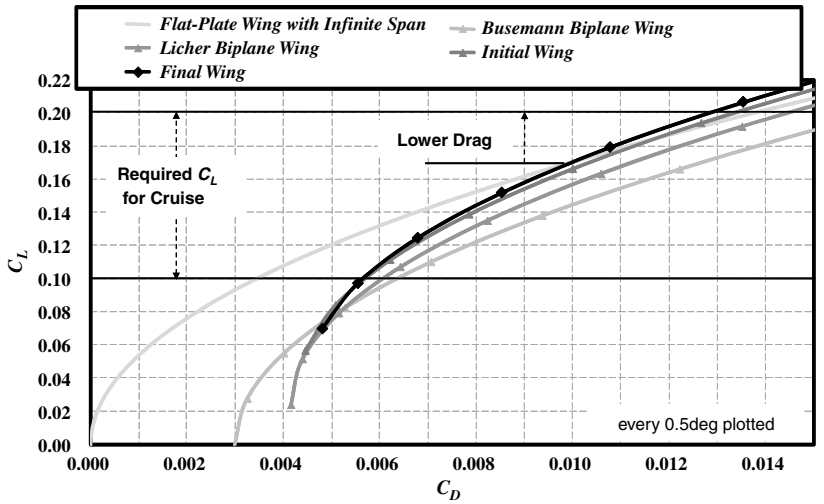

Fig. 31 Drag polar diagram of three-dimensional biplane wings and single flat-plate wing with an infinite span.

three-dimensional flat-plate wing with an infinite span, which has only wave drag due to lift as drag. The final wing achieves lower drag than the three-dimensional flat-plate wing with an infinite span at $C_L > 0.17$. It is notable that a three-dimensional biplane wing has sufficient thickness and also lower drag than that of the three-dimensional zero-thickness single flat-plate wing with an infinite span in the range of the cruise condition, $0.1 < C_L < 0.2$.

VI. Conclusions

To attain supersonic transport characterized by low-drag, the concept of the Busemann biplane was adopted. The extension of biplane airfoils to three-dimensional wings was attempted based on two-dimensional biplane analysis. Design Mach number is 1.7, and total thickness-chord ratio is about 0.10. Euler simulations were conducted in this study. In three-dimensional supersonic biplane wings, there are areas affected by the Mach cones originated from the wing tips. The Mach cones cause a large amount of drag. For control of the increase of the drag due to the Mach cones, planforms of three-dimensional biplane wings were examined. A tapered wing was selected to decrease the wing tip areas affected by the Mach cones, where the largest amount of drag was produced. A two-dimensional inversely designed biplane airfoil, which has been discussed in [9], was applied to the three-dimensional tapered wing, and the inverse-design method was employed at 10 span stations to further improve the aerodynamic performance. The taper ratio and the aspect ratio of the biplane wing were 0.25 and 5.12, respectively. The three-dimensional tapered wing as an initial model for the inverse-design approach, the section airfoil configuration of which is that of the two-dimensional designed biplane airfoil, achieved performances of $C_L = 0.111$, $C_D = 0.00621$, and $L/D = 17.9$.

As prescribing the target pressure distributions for three-dimensional wing design, we tried to remove the pressure peaks around the midchord and create more lift at the trailing edge. Then we tried to extend the C_p distributions obtained from the mid wing. After 14 iterations of the design procedure had been conducted on both the upper and lower elements, every section of the biplane wing was examined to determine if a certain section performed better than it had at the initial stage of the design. When the designed wing section at the wing root did not perform better than that from the initial one, the shape of the designed section was replaced by that of the initial section. Finally, the designed configuration of a supersonic biplane wing, with performances of $C_L = 0.125$, $C_D = 0.00678$, and $L/D = 18.4$ was obtained. It realized lower drag than the three-dimensional zero-thickness single flat-plate wing with an infinite span in the range (where C_L is greater than 0.17, i.e., the cruise condition) of the cruise condition $0.1 < C_L < 0.2$.

As for viscous effects, it was already confirmed in two-dimensional cases that the total drag coefficient of a biplane was about one-third of that of a monoplane even though the wet area of a biplane was twice that of a monoplane. In the future, Navier–Stokes simulations will need to be conducted on three-dimensional supersonic biplane wings.

Acknowledgments

We would like to thank S. Obayashi of Tohoku University for his valuable guidance and comments. The present computations were mainly performed using NEC SX-8 of the Advanced Fluid Information Research Center of the Institute of Fluid Science at Tohoku University. I sincerely thank all the staff for their helpful assistance.

References

[1] Busemann, A., "Aerodynamic Lift at Supersonic Speeds," *Luftfahrtforschung*, 12th ed., No. 6, 3 Oct. 1935, pp. 210–220.

[2] Liepmann, H. W., and Roshko, A., *Elements of Gas Dynamics*, Wiley, New York, 1957, pp. 107–123, 389.

[3] Licher, R. M., "Optimum Two-Dimensional Multiplanes in Supersonic Flow," Douglass Aircraft Co., Rept. SM-18688, Jan. 1955.

[4] Moeckel, W. E., "Theoretical Aerodynamic Coefficients of Two-dimensional Supersonic Biplanes," NACA, Rept. TN 1316, June 1947.

[5] Ferri, A., "Experiments at Supersonic Speed on a Biplane of the Busemann Type," translated by M. Flint, Research Triangle Park, Trans. No. 1407, 1944, pp. 1–40.

[6] Kusunose, K., Matsushima, K., Goto, Y., Yamashita, H., Yonezawa, M., Maruyama, D., and Nakano, T., "A Fundamental Study for the Development of Boomless Supersonic Transport Aircraft," AIAA Paper 2006-0654, Jan. 2006.

[7] Kusunose, K., Matsushima, K., Goto, Y., Maruyama, D., Yamashita, H., and Yonezawa, M., "A Study in the Supersonic Biplane Utilizing its Shock Wave Cancellation Effect," *Journal of the Japan Society for Aeronautical and Space Sciences*, Vol. 55, No. 636, 2007, pp. 1–7 (in Japanese).
doi:10.2322/jjsass.55.1

[8] Kusunose, K., Matsushima, K., Obayashi, S., Furukawa, T., Kuratani, N., Goto, Y., Maruyama, D., Yamashita, H., and Yonezawa, M., *Aerodynamic Design of Supersonic Biplane: Cutting Edge and Related Topics*, The 21st Century Center of Excellence (COE) Program International COE of Flow Dynamics Lecture Series, Vol. 5, Tohoku Univ. Press, Sendai, Japan, 2007.

[9] Maruyama, D., Matsushima, K., Kusunose, K., and Nakahashi, K., "Aerodynamic Design of Biplane Airfoils for Low Wave Drag Supersonic Flight," AIAA Paper 2006-3323, June 2006.

[10] Matsushima, K., Kusunose, K., Maruyama, D., and Matsuzawa, T., "Numerical Design and Assessment of a Biplane as Future Supersonic Transport," *Proceedings of the 25th ICAS Congress*, ICAS Paper 2006-3.7.1, Hamburg, Sept. 2006.

[11] Yonezawa, M., Yamashita, H., Obayashi, S., and Kusunose, K., "Investigation of Supersonic Wing Shape Using Busemann Biplane Airfoil," AIAA Paper 2007-0686, Jan. 2007.

[12] Maruyama, D., Matsuzawa, T., Kusunose, K., Matsushima, K., and Nakahashi, K., "Consideration at Off-Design Conditions of Supersonic Flows Around Biplane Airfoils," AIAA Paper 2007-0687, Jan. 2007.

[13] Yamashita, H., Yonezawa, M., Obayashi, S., and Kusunose, K., "A Study of Busemann-Type Biplane for Avoiding Choked Flow," AIAA Paper 2007-0688, Jan. 2007.

[14] Kuratani, N., Ogawa, T., Yonezawa, M., Yamashita, S., and Obayashi, S., "Experimental and Numerical Study on Aerodynamic Characteristics of Supersonic Biplane in Whole Speed Range," *Proceedings of the 2nd European Conference for Aerospace Sciences*, Paper 2.05.02, July 2007.

[15] Maruyama, D., Matsushima, K., Kusunose, K., and Nakahashi, K., "Aerodynamic Design of Three-Dimensional Low Wave-Drag Biplanes Using Inverse Problem Method," AIAA Paper 2008-0289, Jan. 2008.

[16] Kashitani, M., Yamaguchi, Y., Sunahara, E., and Kitano, H., "Preliminary Study on Side-Wall Boundary Layers in Transonic Shock Tube Airfoil Testing," AIAA Paper 2008-0850, Jan. 2008.

[17] Odaka, Y., and Kusunose, K., "Interference Effect of Body on Supersonic Biplane Wings," *Proceedings of the 40th Fluid Dynamics Conference/Aerospace Numerical Simulation Symposium 2008*, Paper 1B10, June 2008 (in Japanese).

[18] Maruyama, D., Kusunose, K., and Matsushima, K., "Aerodynamic Characteristics of a Two-Dimensional Supersonic Biplane, Covering its Take-Off to Cruise Conditions," *Shock Waves*, Vol. 18, No. 6, 2009, pp. 437–450.

[19] Tan, H. S., "The Aerodynamics of Supersonic Biplanes of Finite Span," Wright Air Development Center, Rept. 52-276, Dec. 1950.

[20] Lomax, H., and Sluder, L., "A Method for the Calculation of Wave Drag on Supersonic-Edged Wings and Biplanes," NACA, Rept. TN 4232, Mar. 1958.

[21] Cheng, H. K., "A Revisit to Supersonic-Flow Theory in the Early Fifties," AIAA, Paper 88-3799, July 1988.

[22] White, F. M., *Viscous Fluid Flow*, 2nd ed., McGraw–Hill, New York, 1991, pp. 429–430.

[23] Spalart, P. R., and Allmaras, S. R., "A One-Equation Turbulence Model for Aerodynamic Flows," AIAA, Paper 92-0439, Jan. 1992.

[24] Nakahashi, K., Ito, Y., and Togashi, F., "Some Challenge of Realistic Flow Simulations by Unstructured Grid CFD," *International Journal for Numerical Methods in Fluids*, Vol. 43, No. 6–7, 2003, pp. 769–783.
doi:10.1002/fld.559

[25] Ito, Y., and Nakahashi, K., "Surface Triangulation for Polygonal Models Based on CAD Data," *International Journal for Numerical Methods in Fluids*, Vol. 39, No. 1, 2002, pp. 75–96.
doi:10.1002/fld.281

[26] Sharov, D., and Nakahashi, K., "Reordering of Hybrid Unstructured Grids for Lower–Upper Symmetric Gauss–Seidel Computations," *AIAA Journal*, Vol. 36, No. 3, 1998, pp. 484–486.
doi:10.2514/2.392

[27] Matsushima, K., Maruyama, D., and Matsuzawa, T., "Numerical Modeling for Supersonic Flow Analysis and Inverse Design," *Proceedings of Lectures and Workshop International: Recent Advances in Multidisciplinary Technology and Modeling*, SS05-2.1, May 2007, pp. 185–194.